



A Multimessenger Mass Determination Method for LISA Neutron Star–White Dwarf Binaries

Kaye Jiale Li¹, Jane SiNan Long^{1,2}, Kinwah Wu^{1,2}, and Albert K. H. Kong²¹ Mullard Space Science Laboratory, University College London, Holmbury St Mary, Surrey, RH5 6NT, UK; j-li.19@ucl.ac.uk, sinan.long.23@ucl.ac.uk² Institute of Astronomy, National Tsing Hua University, Hsinchu 30013, Taiwan (ROC); akong@gapp.nthu.edu.tw

Received 2024 May 27; revised 2025 March 11; accepted 2025 March 14; published 2025 April 23

Abstract

Determining the masses of neutron stars (NSs) accurately improves our understanding of the NS interior and complicated binary evolution. However, the masses of the systems are degenerate with the orbital inclination angle when using solely gravitational waves (GWs) or electromagnetic measurements, especially for face-on binaries. Taking advantage of both GWs and optical observations for LISA NS–white dwarf (WD) binaries, we propose a mass determination method utilising multimessenger observational information. By combining the binary mass function obtained from optical observations and a GW mass function, which we introduce, derived from GW observations, we demonstrate how we can set improved constraints on the NS mass and break the degeneracy in the mass and viewing inclination determination. We further comment on the universal relation of the error bar of the GW mass function versus the GW signal-to-noise ratio and propose a simple method for estimating the capability of using GW observations for mass determination with LISA. We show that for ultracompact NS–WD binaries within our Galaxy, the mass of the NS can be constrained to within an accuracy of $\pm 0.2 M_{\odot}$ with the proposed method.

Unified Astronomy Thesaurus concepts: Neutron stars (1108); Compact binary stars (283); Gravitational waves (678)

1. Introduction

Neutron stars (NSs) are composed of the densest matter known to date, and their mass density is inaccessible in laboratory experiments. The masses of NSs are around $1\text{--}2 M_{\odot}$, and their upper limit is set by the ability of the forces of quantum nature to counteract the NS’s self-gravity. Observations have revealed several massive ($\gtrsim 2 M_{\odot}$) NSs in NS–white dwarf (WD) binaries (P. B. Demorest et al. 2010; J. Antoniadis et al. 2013; H. T. Cromartie et al. 2020; E. Fonseca et al. 2021). These observations have challenged the existence of exotic matter, which typically softens the equation of state (EOS) compared to pure nucleonic matter, thereby lowering the maximum mass an NS can support (M. Baldo et al. 2000; I. Vidaña et al. 2011; H. R. Moshfegh & M. Ghazanfari Mojarraad 2013). A large parameter space for such exotic matter has been ruled out or at least disfavored (see, e.g., P. B. Demorest et al. 2010; P. T. H. Pang et al. 2021). However, models incorporating a condensed quark core remain viable (A. Akmal et al. 1998; M. G. Alford et al. 2013; A. Li et al. 2021; S.-P. Tang et al. 2021), and factors such as many-body corrections to baryon–baryon interactions (A. Akmal et al. 1998; X. R. Zhou et al. 2004; Z. H. Li & H. J. Schulze 2008; M. Ghazanfari Mojarraad & R. Arabsaedi 2016), magnetic fields (Z. Zuraig et al. 2023), differential rotation (P. L. Espino & V. Paschalidis 2019), and finite temperatures (J. M. Lattimer & D. F. Swesty 1991) could alter the upper mass limit. Firmly establishing the mass values for the heaviest NSs will tighten the constraints on the allowed EOS of dense matter and hence the structural models and the internal compositions of the NS

family (J. M. Lattimer & M. Prakash 2004, 2007). It also gives us a means to study the behaviors of complex phases of dense quantum matter under extreme pressure and gravity (S. S. Avancini et al. 2008; G. Baym et al. 2018; H. Tan et al. 2022).

Compact NS–WD binaries in our Galaxy are candidate sources for the space-borne gravitational-wave (GW) detector LISA. They could be formed through several channels. For instance, some may descend from low-mass/intermediate-mass X-ray binaries (LMXBs/IMXBs), consisting of an NS accreting matter from a low- or intermediate-mass giant (see, e.g., T. M. Tauris & G. J. Savonije 1999) or even a degenerate WD companion (see, e.g., A. V. Tutukov & L. R. Yungel’Son 1993). They may also be products of dynamical few-body interactions occurring in very dense stellar environments, e.g., cores of dense stellar clusters. The Galactic population of NS–WD binaries is highly uncertain. It is estimated to range from a few to a few hundreds within LISA detection sensitivity, based on population synthesis models or X-ray luminosity function (M. J. Benacquista et al. 2001; G. Nelemans et al. 2001; A. Cooray 2004; W.-C. Chen et al. 2020; V. Korol et al. 2024). The NS–WD binaries, be they in the detached or semi-detached configuration, with orbital evolution driven by angular momentum loss through gravitational radiation (see B. Paczyński 1971), can provide clean constraints on the masses of component stars through multimessenger observations. The compact nature of the WD companion allows the NS–WD binaries to remain detached, even when their orbital period, P_{orb} , evolves to as short as about $\lesssim 10$ minutes (T. M. Tauris 2018; H.-L. Chen et al. 2021, 2022; S. Yu et al. 2021). These NS–WD binaries naturally emit GWs. The frequencies of their GWs are expected to be from 0.5 to 3 mHz, which fall within the detectable range of LISA (see P. Amaro-Seoane et al. 2017). Multimessenger observations of NS–WD binaries in GW and electromagnetic (EM) waves will give us opportunities to probe the physics of high-density matter in strong gravity in addition to enhancing



Original content from this work may be used under the terms of the [Creative Commons Attribution 4.0 licence](https://creativecommons.org/licenses/by/4.0/). Any further distribution of this work must maintain attribution to the author(s) and the title of the work, journal citation and DOI.

our understanding of the nature, the dynamics, and the origins of NS–WD binaries.

The focus of this study is to derive tighter constraints on the masses of the NSs in NS–WD binaries detectable by LISA. We specifically introduce a GW mass function, which is constructed using information from GW observations. This is complementary to the conventional binary mass function, which is derived from optical photometry or spectroscopy or other EM/photonic observations. We use the GW analysis pipeline `gbmcmc` (T. B. Littenberg et al. 2020a) to generate mock LISA data for parameter estimations. Using the results from Markov Chain Monte Carlo sampling and the two mass functions, which are almost diagonal, we can constrain the orbital inclinations and hence establish the masses of the NSs. We organize the paper as follows. The methodology and the procedures are presented in Section 2 and the results in Section 3. We discuss our findings in Section 4. We also comment on the astrophysics of the target binaries. A short summary is given in Section 5.

2. Method

2.1. Signal-to-noise-ratio Threshold for GW Sources

Consider a binary system consisting of an NS of m_{ns} and a low-mass WD of m_c orbiting around each other with a period P_{orb} . The orbital revolution of the binary leads to the emission of a GW, and the GW is characterized by a frequency $f_{\text{GW}} \equiv 2/P_{\text{orb}}$. The loss of orbital energy and angular momentum caused by the GW emission bring the stars in the binary closer, which in turn shortens P_{orb} and increases f_{GW} . The rate of change in f_{GW} is given by

$$\begin{aligned} \dot{f}_{\text{GW}} &= \frac{96}{5} \frac{G^{5/3}}{c^5} \pi^{8/3} \mathcal{M}^{5/3} f_{\text{GW}}^{11/3} \\ &\approx 1.8 \times 10^{-11} \left(\frac{\eta}{0.3} \right) \left(\frac{M}{2.6 M_{\odot}} \right)^{5/3} \left(\frac{1 \text{ hr}}{P_{\text{orb}}} \right)^{11/3} \text{ Hz yr}^{-1} \end{aligned} \quad (1)$$

(see, e.g., M. Maggiore 2008), where $M = m_{\text{ns}} + m_c$ is the total mass of the binary, $\eta = (m_c m_{\text{ns}})/(m_{\text{ns}} + m_c)^2$ is the symmetric mass ratio, and

$$\mathcal{M} \equiv \frac{(m_c m_{\text{ns}})^{3/5}}{(m_{\text{ns}} + m_c)^{1/5}} \quad (2)$$

is the chirp mass.

For the parameters of interest in this study, the drift in frequency is about $\Delta f_{\text{GW}} \approx 1 \times 10^{-11}$ Hz over a period of 4 yr (the expected LISA mission lifetime). This value is much smaller than f_{GW} . The GW from the system is therefore practically quasi-monochromatic. Following L. S. Finn & K. S. Thorne (2000), we define the characteristic amplitude of the GW as $h_c \equiv h_o \sqrt{2f^2/\dot{f}}$, where $h_o \equiv \sqrt{\langle h_+^2 + h_{\times}^2 \rangle} = I(\iota) \sqrt{G\dot{E}/c^3}/(\pi df)$ is the rms amplitude of the two polarizations averaged over one GW period. The prefactor $I(\iota)$ accounting for the effect of the inclination angle, which is the rms of the angular part of h_+ and h_{\times} , is given by

$$I(\iota) \equiv \sqrt{\frac{5}{4}} \sqrt{\cos^2 \iota + \left(\frac{1 + \cos^2 \iota}{2} \right)^2}, \quad (3)$$

which is normalized such that $\int (d\Omega/4\pi) I^2(\iota) = 1$. The signal-to-noise ratio (SNR) of this quasi-monochromatic GW is

$$\text{SNR} = \sqrt{\int_{-\infty}^{\infty} d(\ln f) \left(\frac{h_c(f)}{h_n(f)} \right)^2} \approx \frac{\sqrt{2fT} h_o}{h_n(f)} \quad (4)$$

(É. É. Flanagan & S. A. Hughes 1998; L. S. Finn & K. S. Thorne 2000; C. J. Moore et al. 2015; T. Robson et al. 2019), where $h_n(f) \equiv \sqrt{f S_n(f)}$ is the sky-averaged rms noise at frequency f , and T is the observational time. $S_n(f)$ is the one-sided, sky-averaged power spectral density of the detector at frequency f .

We may take the sensitivity curve as

$$\begin{aligned} S_n(f) &= \frac{10}{3L^2} \left\{ P_{\text{OMS}} + 2 \left[1 + \cos^2 \left(\frac{f}{f_*} \right) \right] \frac{P_{\text{acc}}}{(2\pi f)^4} \right\} \\ &\quad \times \left[1 + \frac{6}{10} \left(\frac{f}{f_*} \right)^2 \right] \end{aligned} \quad (5)$$

(T. Robson et al. 2019). Here, $L = 2.5$ Gm and $f_* = c/(2\pi L) = 19.09$ mHz. The single-test-mass acceleration noise single-link optical metrology noise P_{acc} and P_{OMS} are then

$$\begin{cases} P_{\text{acc}} = 9 \times 10^{-30} \left[1 + \left(\frac{0.4 \text{ mHz}}{f} \right)^2 \right] \left[1 + \left(\frac{f}{8 \text{ mHz}} \right)^4 \right] \frac{\text{m}^2}{\text{Hz s}^4} ; \\ P_{\text{OMS}} = 2.25 \times 10^{-22} \left[1 + \left(\frac{2 \text{ mHz}}{f} \right)^4 \right] \frac{\text{m}^2}{\text{Hz}}, \end{cases} \quad (6)$$

to be consistent with the `gbmcmc` package used in this study.³

Based on the formula of the SNR in Equation (4), we define an effective GW strain $h_e = \sqrt{2fT} h_o = \sqrt{2\mathcal{N}_{\text{cyc}}} h_o$, where \mathcal{N}_{cyc} is the number of wave cycles detected within the observational time T , which is the same as that adopted in W.-C. Chen et al. (2020). The effective GW strain is then

$$\begin{aligned} h_e &= I(\iota) \sqrt{2\mathcal{N}_{\text{cyc}}} \frac{1}{\pi df} \sqrt{\frac{G\dot{E}}{c^3}} \\ &= I(\iota) \frac{8}{\sqrt{5}} \frac{G^{5/3}}{dc^4} \pi^{2/3} \mathcal{M}^{5/3} f^{2/3} \sqrt{\mathcal{N}_{\text{cyc}}} \\ &\approx 3 \times 10^{-20} I(\iota) \left(\frac{30 \text{ min}}{P_{\text{orb}}} \right)^{7/6} \left(\frac{M}{(2/5)^{1/5} M_{\odot}} \right)^{5/3} \\ &\quad \times \left(\frac{T}{4 \text{ yr}} \right)^{1/2} \left(\frac{10 \text{ kpc}}{d} \right), \end{aligned} \quad (7)$$

and the SNR can be visually determined by how far this effective strain is above the noise amplitude $h_n(f)$.

While it is conventional to set $\text{SNR} = 5$ as the criterion of detection, this threshold is merely representative. Depending on the time-delay interferometry (TDI) channels considered, whether sky averaging has been performed and how it has been performed, the amplitude of the Galactic confusion noise, and whether the orbital orientation is averaged out, the SNR value of the exact same system could differ by a factor of a few. For example, the package `gbmcmc` (T. B. Littenberg et al. 2020a) has a more detailed definition of SNR (see T. B. Littenberg & N. J. Cornish 2019), using a combination of the A and E channels with realistic responses to different sky locations, polarization, and inclination angles. For simplicity,

³ The noise parameters are adapted from the LISA Data Challenges git: <https://gitlab.in2p3.fr/LISA/LDC/-/blob/master/ldc/lisa/noise/noise.py>.

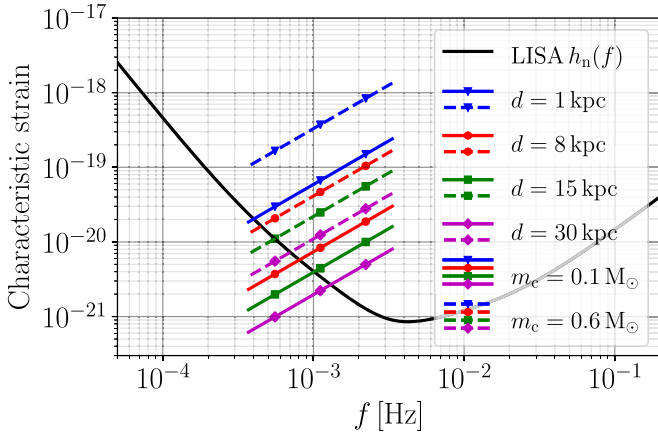


Figure 1. The range of the inclination-angle-averaged effective GW strain of the binary system with $m_{\text{ns}} = 2.0 M_{\odot}$ and $m_c = 0.1, 0.6 M_{\odot}$ at $d = 1, 8, 15$, and 30 kpc. Each line represents a specific type of binary system of the same m_c and d , with the orbital period P_{orb} spanning from 10 to 90 minutes. The three nodes are marked at $P_{\text{orb}} = 60, 30, 15$ minutes, from left to right, respectively. The integration time of the observations is set to be 4 yr. The LISA sensitivity curve is defined in Equation (5).

we have considered two X -channels and averaged over the source’s sky position and detector orientation angle. For the system we consider in this work, our SNR definition in Equation (4) is consistent in number with SNR(gbmcmc), with a difference of $\leq 20\%$, mainly depending on the sky position. To account for this subtle difference in definitions across the literature, we relax this criterion to $\text{SNR} = 2$ and consider a wider range of systems, including those with $2 < \text{SNR} < 5$. Nevertheless, the SNR—or sometimes SNR(gbmcmc) as calculated by the gbmcmc package—of each system will be listed to indicate the possibility of it being detected.

In this study, we consider NS–WD binaries with orbital period $P_{\text{orb}} = 10 - 60$ minutes, which is within LISA’s sensitivity range. The parameter choice extends toward lower frequencies, as systems with longer periods have longer lifetimes compared to more compact systems, thus dominating the population. The distance range for these systems is chosen to be $d = 1 - 30$ kpc, covering our entire Galaxy. In particular, we choose hypothetical systems very close by, to study parameter degeneracy and demonstrate the universality of our findings for high-SNR systems. The existence of such systems within our Galaxy is discussed in Section 4.2. Without losing generality, we assume that the binary has a circular orbit. The mass of the NS is $2 M_{\odot}$ ⁴ and the mass of the companion star is within the range $m_c = 0.1 - 0.6 M_{\odot}$, although the majority of our results can be extended to a wider parameter range. Figure 1 illustrates the effective GW strains of the NS–WD binaries, for a range of distances, orbital periods, and companion masses. The LISA sensitivity curve is included in the graph for comparison.

⁴ The existence of $2 M_{\odot}$ NSs is supported by observations of NS–WD binaries (P. B. Demorest et al. 2010; J. Antoniadis et al. 2013; H. T. Cromartie et al. 2020; E. Fonseca et al. 2021), motivating our choice of this value. In the literature, $2 M_{\odot}$ is often used as a benchmark for identifying the existence and properties of exotic matter (A. Akmal et al. 1998; J. M. Lattimer & M. Prakash 2011). However, exotic matter can still support NSs exceeding $2 M_{\odot}$, with a critical threshold likely a few tenths of a solar mass higher—though this remains highly model-dependent and complex (see, e.g., P. Char & S. Banik 2014; Z. Zuraiq et al. 2023). For simplicity, we adopt this convention while noting that our main result is insensitive to the specific choice.

2.2. Parameter Estimation Method

NS–WD binaries have the potential to be identified through EM observations before LISA is launched, contributing to the family of verification binaries for LISA (A. Stroeer & A. Vecchio 2006; V. Korol et al. 2017; T. Kupfer et al. 2018, 2024; K. B. Burdge et al. 2019, 2020; M. Kilic et al. 2021; E. Finch et al. 2023; P. T. Johnson et al. 2023). Alternatively, if the WD companion is too faint for detection in optical surveys, GW observations could offer localization information for the binary, enabling targeted follow-up searches. In this study, we assume that the binary has been identified through optical observations, either before or after GW identification. Through spectroscopic analysis, supplemented with photometric analysis, the orbital periods P_{orb} and phase-resolved radial velocities K of the WD are measured and are then used to construct the binary mass function:

$$f(m) = \frac{P_{\text{orb}} K^3}{2\pi G} = \frac{m_{\text{ns}}^3 \sin^3 \iota}{(m_{\text{ns}} + m_c)^2}. \quad (8)$$

Currently, there have been no confirmed identifications of our target compact (10–60 minutes) NS–WD binaries.⁵ Estimating the uncertainty in determining the binary mass function poses a nontrivial challenge. This uncertainty arises from factors such as the data quality, as well as the modeling of the WD’s brightness variations due to tidal effects and/or pulsar irradiation. Given these complexities, we find it impractical to estimate the uncertainty directly for an unspecified system over a multidimensional parameter space. Instead, focusing on GW observations, we assign specific values to the binary mass function uncertainty (i.e., 5%–20%) to assess the sensitivity of mass estimates under these conditions.

For the GW part, we made use of the package gbmcmc (T. B. Littenberg et al. 2020b), to perform mock parameter estimation of such binary systems with different inclination angles, orbital periods, and distances. Each binary is fitted with typically eight parameters, including the orbital frequency f , frequency derivative \dot{f} , GW amplitude A , inclination angle ι , polarization angle ψ , initial orbital phase ϕ of the GW, and sky localization, where

$$A \equiv \frac{2}{d} \frac{G^{5/3}}{c^4} (\pi f)^{2/3} \mathcal{M}^{5/3}. \quad (9)$$

We have excluded noise in the mock data, so as to derive a clearer degeneracy between system parameters. In this analysis, we have assumed such a system to be readily detected via EM observations with known sky location and orbital frequency and hence f . The prior of the polarization angle and initial orbital phase is uniform in $[0, \pi]$ and $[0, 2\pi]$, respectively. We

⁵ The absolute brightness of WDs is $M_V \sim 11.5$ (see, e.g., A. M. Mickaelian et al. 2022). This corresponds to the visual magnitude $V \approx 26$ at a distance of 8 kpc. The 8 m class ESO Very Large Telescopes are capable of observing sources of $V \approx 27$ with sensible SNRs at an integration time of 1 hr (see V. Reddy et al. 2019). While observation for our target NS–WD binaries at a distance exceeding about 4 kpc with reliable photometric determination of periodic variations is beyond the capacity of current ground-based telescopes, with the coming of the 30 m class telescopes, such as the Extremely Large Telescope and the Thirty Meter Telescope, resolving 10 minutes photometric variations at $V \approx 26$ would be achievable for hours of integration time. The simple estimate above has not taken account of important local effects, such as the night sky brightness and atmospheric scintillations. All these would restrict the size of the observational volume for the target binaries to reside in. We may be able to circumvent these in space-based observations, where the night sky brightness, seeing, and other atmospheric effects would not be present.

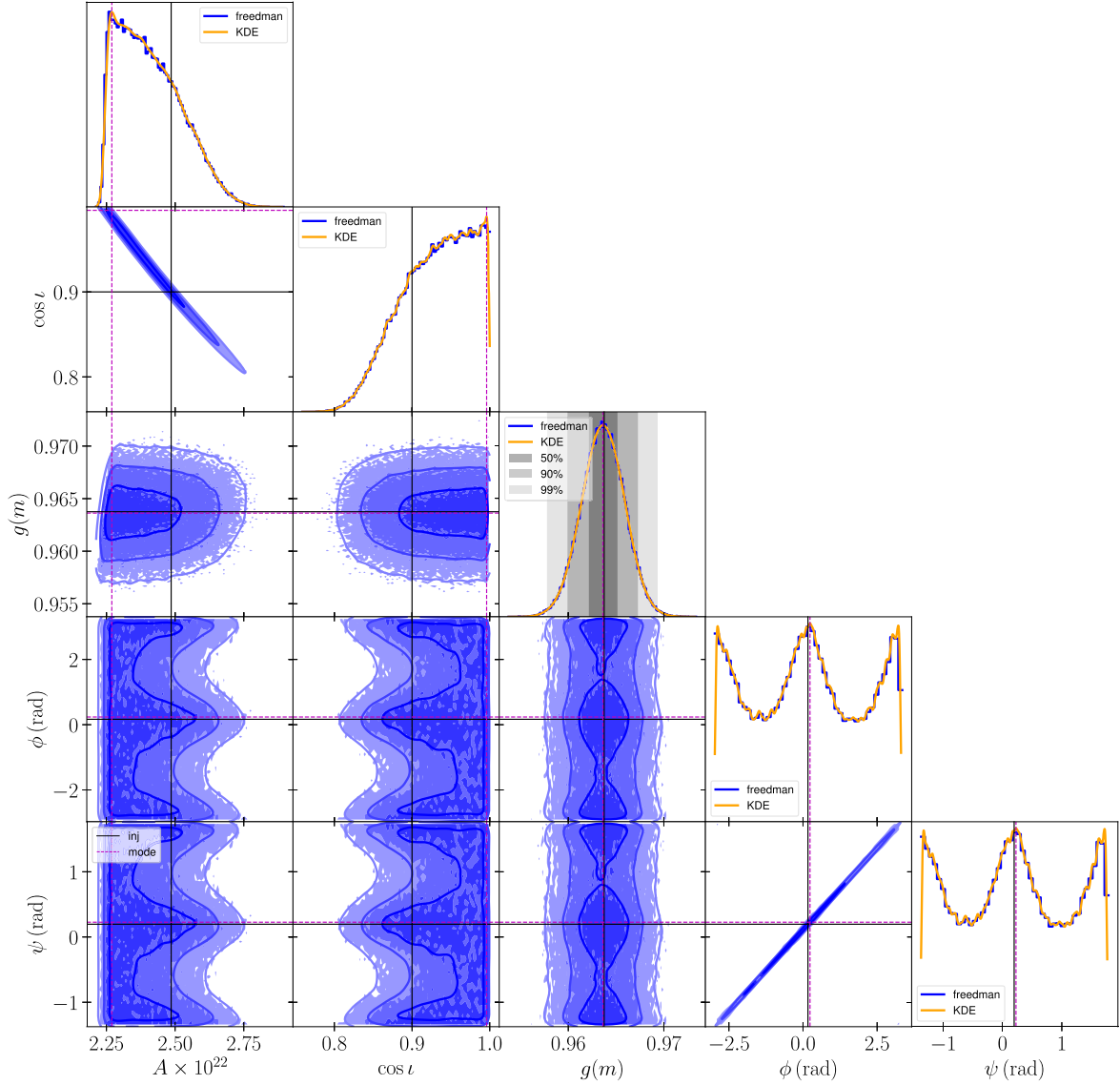


Figure 2. The parameter estimation of the GW emitted by a binary system with $m_c = 0.5 M_\odot$, $P_{\text{orb}} = 15$ minutes, and $\cos i = 0.9$ (nearly face-on) located 3 kpc away. The detection time is 4 yr. The SNR of this system is ≈ 260 . The contour lines represent the 50%, 90%, and 99% confidence intervals. The histogram is calculated using the *astropy* package (Astropy Collaboration et al. 2022) and the kernel density estimation (KDE) is calculated by the *getdist* package (A. Lewis 2019).

restrict our study to the prograde orbit and set the prior on the inclination angle such that $\cos i$ is uniform in $[0, 1]$. The prior amplitude A is log-uniform between $\ln A = -60$ and $\ln A = -45$.

In the mock parameter estimation, the system is assumed to be located at $\sin(\text{latitude}) = 0.6080$ and longitude $= 2.9737$ in solar system barycenter ecliptic coordinates, and it consists of an NS with $2 M_\odot$ and a companion with $m_c = 0.1\text{--}0.6 M_\odot$, with an observational duration of the GW signal of 4 yr. The system is assumed to have negligible accretion, such that $\dot{f} = \dot{f}_{\text{GW}} \ll f/4$ yr, and the source is essentially monochromatic. In this study, we aim at demonstrating the capability of GW observations and hence have adopted a simplified model, by assuming that the companion mass and binary distance are known a priori from previous EM observations (see the Appendix for a detailed discussion). With the information of m_c and distance d known, the mass of the NS can be exactly determined from a given A by combining Equations (2) and (9). In practice, both the companion mass and the distance would be measured with an error bar. For

such a monochromatic source, the distance is completely degenerate with the chirp mass. Therefore, the uncertainty of the distance can be translated into the uncertainty of the GW chirp mass via error propagation.

The error propagation for the companion mass is more subtle, as it appears in both the binary mass function and GW amplitude. We will show how the error of the companion mass affects the error of the NS's mass in the Appendix.

While it is straightforward to calculate the system's chirp mass from the GW amplitude A using Equation (9), A is not necessarily a good parameter, due to its degeneracy with the inclination angle in the GW detection. The two observed polarization modes $h_+ \propto A(1 + \cos^2 i)/2$ and $h_\times \propto A \cos i$, suggest that a system with larger A and larger inclination angles can be mistaken as a system with smaller A and smaller inclination angles. Significant degeneracy appears even for signals with large SNR when the system is close to face-on. For example, Figure 2 shows the parameter estimation for an unrealistic injected signal emitted by a binary with

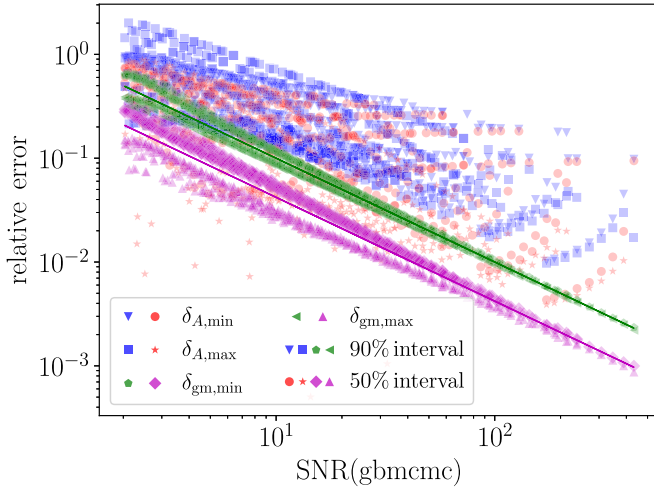


Figure 3. The relative errors of the parameters A and $g(m)$ vs. the SNR of the system, at confidence intervals of 50% and 90%, respectively. The upper and lower error bars of $g(m)$ are defined as $\delta_{g,m,\max} \equiv (\max g(m) - g(m)_0)/g(m)_0$, $\delta_{g,m,\min} \equiv (g(m)_0 - \min g(m))/g(m)_0$, and similarly for A . Some $\delta_{A,\max}$ values are missing, as the strong degeneracy between A and $\cos \iota$ has led to $\max A < A_0$, as demonstrated in Figure 2. The relative errors of $g(m)$ roughly follow a power-law relation with respect to the SNR, whereas the error bars of A have large scatters. The solid lines represent the power-law relations reported in Equation (11), which are derived by fitting the average of the maximum and minimum relative errors. The data shown are calculated with $m_c = 0.6 M_\odot$ and $P_{\text{orb}} = 20 - 60$ minutes, although the results for other masses and orbital periods are very similar.

$m_c = 0.5 M_\odot$, $P_{\text{orb}} = 15$ minutes, and $\cos \iota = 0.9$ at a distance of 3 kpc. This system has $\text{SNR} \approx 260$ after a 4 yr integration time. The parameter estimation for such a luminous system is expected to be very precise, but as shown by the 1D marginalized probability density function (PDF) of A and $\cos \iota$, both PDFs differ significantly from a bell-shaped distribution and the locations of the maximum posteriors mismatch the true values. This degeneracy motivates the definition of a new parameter that combines the information of both amplitude and inclination angle.

We define a GW mass function from the GW measurement, similar to the binary mass function from measurements of the radial velocity variation (e.g., Equation (8)), as

$$g(m) = \left[\frac{Ad}{2(\pi f)^{2/3}} \frac{c^4}{G^{5/3}} \sqrt{\cos^2 \iota + \left(\frac{1 + \cos^2 \iota}{2} \right)^2} \right]^{3/5} \\ = \frac{(m_{\text{ns}} m_c)^{3/5}}{(m_{\text{ns}} + m_c)^{1/5}} \left[\cos^2 \iota + \left(\frac{1 + \cos^2 \iota}{2} \right)^2 \right]^{3/10}. \quad (10)$$

Similar to that of the binary mass function, the first equals sign shows how the GW mass function is derived from direct observation parameters, while the second equals sign indicates its relation to the intrinsic binary parameters. Here, A and $\cos \iota$ are obtained from GW parameter estimation, while f and d are known a priori from EM observations. This GW mass function is proportional to $\langle h_+^2 + h_\times^2 \rangle^{3/10}$, taking into account the fact that LISA measures a combination of h_+ and h_\times as it rotates in space. As shown in the bottom right panel of Figure 2, the PDF of the GW mass function has a nice symmetrical bell shape, as opposed to the PDFs of A and $\cos \iota$, which are not as meaningful when viewed individually.

The GW mass function admits advantages in the parameter estimation involving multimessenger observations, regardless of the orbital configuration of the NS–WD binary. The

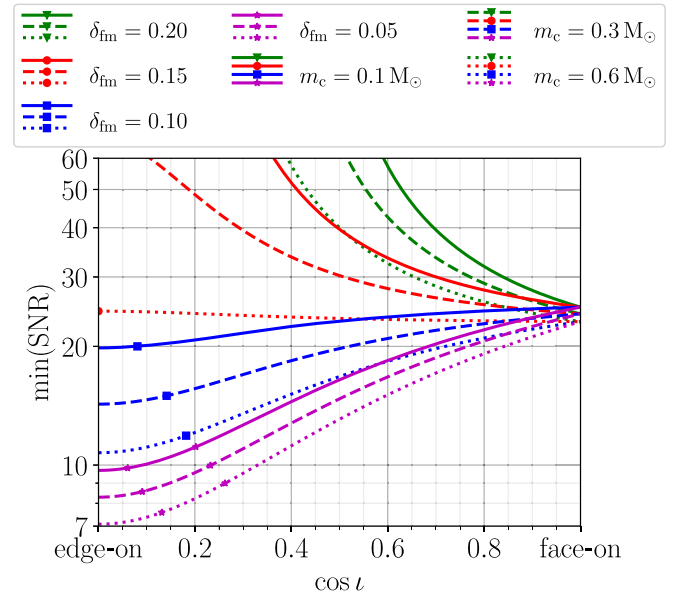


Figure 4. The minimum SNR of the NS–WD binaries required to achieve a measurement of $m_{\text{ns}} = (2 \pm 0.2) M_\odot$ for different companion masses and different measurement accuracies of $\delta_{f,m}$. The markers on each line represent the values of $\cos \iota$ below which the lower bound of m_{ns} placed by $f(m)_{\text{min}}$ alone is equivalent to or better than $1.8 M_\odot$. From right to left, the lower bound due to $f(m)_{\text{min}}$ alone is 1.8 and $1.9 M_\odot$. For some lines, some markers on the left are missing when their best constraints cannot reach the $1.9 M_\odot$ level.

accuracy of the parameter estimation of $g(m)$ follows a simple relation with the SNR of the binary system, particularly at high SNRs. Figure 3 compares the accuracy of the parameter estimation for A and $g(m)$ achievable for NS–WD binaries. Compared with that of A , the relative size of the confidence interval (i.e., the error bar) of $g(m)$ roughly follows a power-law relation with the SNRs of the system. We define $g(m)_{\text{max,min}} = g(m)_0(1 \pm \delta_{g,m})$, such that $g(m)_0$ represents the true value of the GW mass function. The averaged relative error of $\delta_{g,m}$ is reasonably well fitted by the following relations:

$$\begin{cases} \delta_{g,m,50\%} \approx 0.042 \left(\frac{10}{\text{SNR}} \right); \\ \delta_{g,m,90\%} \approx 0.10 \left(\frac{10}{\text{SNR}} \right), \end{cases} \quad (11)$$

which are appropriate for NS–WD binaries with $\text{SNR} \in [3, 400]$. This relation has been validated across a range of companion masses, distances, inclination angles ($\cos \iota = 0.1 - 0.9$), orbital periods ($P_{\text{orb}} = 10 - 60$ minutes), and amplitudes ($A \in [3 \times 10^{-23}, 7 \times 10^{-22}]$), provided the SNR falls within this range. However, caution is advised when applying this relation, as elaborated at the end of this section. As shown in Figure 3, the relative error of $g(m)$ is almost always smaller than that of A at the same confidence interval. For a nearly-edge-on system with $\cos \iota \sim 0$, the relative error bar of $g(m)$ is about three-fifths of that of A , as a consequence of $g(m) \propto A^{3/5}$, except for when $\text{SNR}(\text{gbmcmc}) \leq 3$. For a nearly-face-on system, the relative error bar of A is much larger than that of $g(m)$, as a consequence of the strong degeneracy between A and $\cos \iota$ (see Figure 2).

Deviation from the simple power-law relation is anticipated at low SNR, leading to a more stringent upper bound $\delta_{g,m,\max}$ and a less restrictive lower bound $\delta_{g,m,\min}$. This outcome is a consequence of the log-uniform distribution of the prior for parameter A .

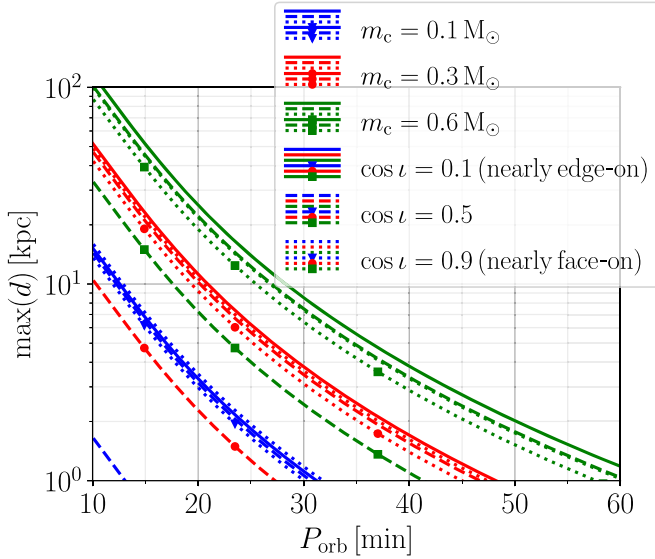


Figure 5. The maximum distance of the NS-WD binary for probing a measurement of $m_{\text{NS}} = 2 \pm 0.2 M_{\odot}$. The unmarked lines represent cases with $\delta_{\text{fm}} = 5\%$ and the marked lines represent cases with $\delta_{\text{fm}} = 20\%$. It is important to highlight that, for cases with $\cos i = 0.1$ and $\delta_{\text{fm}} = 5\%$, the lower bound exceeds $1.8 M_{\odot}$.

For such low-SNR systems, noise can significantly distort or completely obscure the power-law relation, highlighting a limitation that requires further investigation. Additionally, this relation assumes prior knowledge of the system’s orbital frequency, distance, and sky location; when these parameters are subject to measurement uncertainty, nontrivial modifications to the relation of Equation (11) are expected. Given the faintness of the WD, distance is likely the limiting factor. Fortunately, its effect on the GW mass function error takes a simple form, as discussed in the Appendix. The impact of the uncertainty in the sky location and orbital frequency could be much more complicated, and we look forward to future study addressing this issue. Overall, the empirical relation in Equation (11) provides a straightforward way of estimating the accuracy of the GW mass function achievable with LISA observations, bypassing the need for mock parameter estimation.

3. Results

3.1. Analytical Estimates of the NS Mass by Two Mass Functions

As both optical observations and analyses of GW detections have indicated, the main issue for binary parameter estimation is the undetermined mass–inclination degeneracy. For a binary system with both optical observations and GW detection, both mass functions can be measured, each subject to an error bar. As we have assumed that the companion mass m_c is known, the maximum mass can be calculated by solving

$$\begin{cases} f(m)_{\text{max}} = \frac{(m_{\text{ns,max}})^3 \sin^3 i}{(m_{\text{ns,max}} + m_c)^2}; \\ g(m)_{\text{max}} = \frac{(m_{\text{ns,max}} m_c)^{3/5}}{(m_{\text{ns,max}} + m_c)^{1/5}} \left[\cos^2 i + \left(\frac{1 + \cos^2 i}{2} \right)^2 \right]^{3/10} \end{cases} \quad (12)$$

simultaneously, and similarly for the minimum mass. In addition to the joint constraint, the binary mass function places

a lower bound on m_{ns} via

$$\frac{(m_{\text{ns,min}})^3}{(m_{\text{ns,min}} + m_c)^2} \geq f(m)_{\text{min}}. \quad (13)$$

For an edge-on system, the variation of the radial velocity is the maximum, leading to a stringent lower bound on the mass. The GW mass function alone also provides an upper bound,

$$\frac{(m_{\text{ns,max}} m_c)^{3/5}}{(m_{\text{ns,max}} + m_c)^{1/5}} \leq 2^{3/5} g(m)_{\text{max}}, \quad (14)$$

which is only relevant for high-SNR systems that are close to an edge-on configuration. For a face-on system, we have $f(m)_{\text{min}} \approx 0$, and the lower bound is trivial.

Using the empirical relation of Equation (11), the minimum GW SNR required to achieve a measurement of (at least) $m_{\text{ns}} = (2 \pm 0.2) M_{\odot}$ at the 90% confidence level is shown in Figure 4.

When $f(m)$ is measured accurately with $\delta_{\text{fm}} \lesssim 10\%$, the minimum SNR required to probe m_{NS} with the same precision is smaller for nearly-edge-on systems. If the binary mass function is measured with $\pm 5\%$ accuracy or smaller, even systems with $\text{SNR} \lesssim 10$ can constrain the NS mass within $\pm 0.2 M_{\odot}$ for optimal system configuration. The lower bound, which is particularly important for constraining the NS internal structure, is usually better than $0.2 M_{\odot}$ for nearly-edge-on systems, primarily due to the constraint imposed by $f(m)_{\text{min}}$ alone. For nearly-face-on systems, the lower bound of the binary mass function $f(m)$ vanishes, and the joint constraint depends mainly on the GW observations. With such precise binary mass function measurements, NS-WD binaries with $\text{SNR} \geq 25$ can determine the mass to within $\pm 0.2 M_{\odot}$, regardless of other orbital parameters. When the binary mass function is measured less accurately with $\delta_{\text{fm}} \geq 10\%$, the preference for the inclination angle is reversed. For a nearly-edge-on configuration, the constraint is primarily determined by $f(m)$. Therefore, when $f(m)$ is measured with large uncertainty, even a perfect measurement of $g(m)$ is insufficient to constrain m_{NS} to within $\pm 0.2 M_{\odot}$. However, it should be noted that if such a system has a sufficiently high SNR, the $A - \cos i$ degeneracy disappears (see, e.g., Figure 6), and the constraint from GW observations alone could be better than $\pm 0.2 M_{\odot}$. This is not captured by Figure 6, which is calculated using the GW mass function via Equation (11).

Interestingly, the minimum SNR for binaries with a heavier companion is smaller than that for a lighter companion. This dependence becomes prominent when $f(m)$ is measured with a 10% error, in which case the minimum SNR for a heavy companion is approximately half that of a lighter companion. As NS-WD binaries with heavier WDs have larger GW amplitudes, this suggests that accurate NS mass measurement prospects lie in such heavy NS-WD binaries. Using Equation (4), the minimum GW SNR can be translated into a relation between the maximum binary distance and orbital period. The result is shown in Figure 5, in which we adopt $\delta_{\text{fm}} = 5\%$, 20% and $\delta_{\text{gm},90\%}$. Due to the dependency of the SNR and minimum SNR on m_c , the probing distance for NS-WD binaries with a heavier companion of $m_c = 0.6 M_{\odot}$ is about 10 times larger than that for a lighter companion with $m_c = 0.1 M_{\odot}$. Assuming a median distance of 10 kpc, NS-WD binaries with $P_{\text{orb}} \lesssim 30$ minutes and a heavy companion (i.e.,

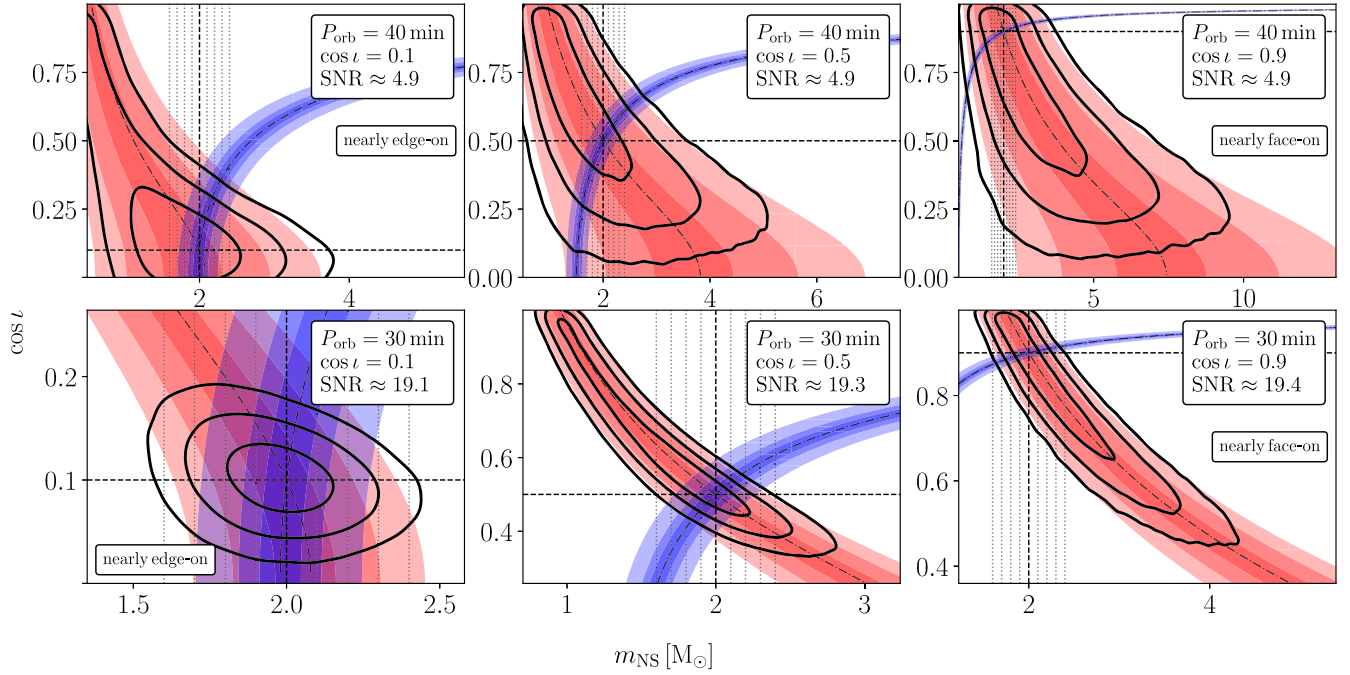


Figure 6. The constraints on the binary parameters for six different binary systems with $m_{\text{ns}} = 2 M_{\odot}$ and $m_c = 0.6 M_{\odot}$ located at (from top left to right) $d = 5.22, 8.11, 12.94$ kpc and (from bottom left to right) $d = 2.99, 4.65, 7.41$ kpc. In each panel, the red strips (which extend from the top left to the bottom right) represent the 50%, 90%, and 99% confidence intervals of the GW mass function $g(m)$ (similar to the shaded region in the last panel of Figure 2). The blue strips (which extend from the bottom left to the top right) represent the $\pm 5\%$, 10% and $\pm 20\%$ error bars of the binary mass function $f(m)$. The black contours represent 2D confidence intervals of 50%, 90%, and 99%. The dashed-dotted lines represent the true values of $f(m)$ and $g(m)$. The horizontal and vertical dashed lines represent the true values of m_{ns} and $\cos \iota$ -s. The vertical dotted lines are reference lines of $m_{\text{ns}} = 1.6\text{--}2.4 M_{\odot}$ with $0.1 M_{\odot}$ spacing.

$m_c \gtrsim 0.6 M_{\odot}$) are the more promising candidates for probing NS mass.

The generic results for Equation (12) are complicated in form, and for ease of computation, we present an approximate formula in the Appendix. The formula is applicable when the relative errors of all quantities are much smaller than unity. Supplemented by the empirical relation outlined in Equation (11), the approximate formula can be employed to estimate the joint constraint on the NS mass for NS–WD binaries with the multimessenger method.

3.2. The Joint Constraints on the NS Mass

The degeneracy between the GW amplitude A and inclination angle translates into a degeneracy between m_{NS} and $\cos \iota$. Figure 6 illustrates this mass-inclination degeneracy from GW and also EM observations for a few NS–WD binaries with $\text{SNR} \approx 5$ and ≈ 20 . The two almost-diagonal strips represent the mass functions $f(m)$ and $g(m)$, respectively. The black contours represent the 50%, 90%, and 99% confidence intervals of a 2D PDF of $\cos \iota - m_{\text{ns}}$. In the following, we will refer to the intersection of the $f(m)$ and $g(m)$ strips as the $g(m) - f(m)$ constraint and the intersection of the $f(m)$ strip and 2D contour of $\cos \iota - m_{\text{ns}}$ from the `gbmcmc` simulation as the $2D - f(m)$ constraint.

The first column of Figure 6 represents the nearly-edge-on cases when the lower bound of m_{ns} from $f(m)_{\text{min}}$ alone outstands (or is comparable to) the joint constraint from the multimessenger method. The upper panel of the first column shows the parameter estimates of a binary system consisting of a $2 M_{\odot}$ NS and a companion star of $m_c = 0.6 M_{\odot}$, revolving around each other with $P_{\text{orb}} = 40$ minutes at a distance of 5.22 kpc and viewed at an inclination $\cos \iota = 0.1$. The system

has $\text{SNR} \approx 5$. When $f(m)$ is measured with $\pm 1\%$, $m_{\text{ns}} < 1.97 M_{\odot}$ and $m_{\text{ns}} > 2.17 M_{\odot}$ can be ruled out at the 90% confidence interval for the $2D - f(m)$ constraint. At the 50% confidence interval, the mass is constrained to be $1.97\text{--}2.08 M_{\odot}$. For a similarly edge-on system with $\text{SNR} \approx 20$ (the lower left panel of Figure 6), δ_{gm} is approximately a quarter of the value of the previous case. Consequently, the upper bound on m_{ns} from the $2D - f(m)$ constraint is $2.03 M_{\odot}$ at the 50% confidence interval and $2.04 M_{\odot}$ at the 90% confidence interval, which are also about a quarter of the values in the previous case. Comparing these two cases reveals that the apparent mass-inclination degeneracy from GW observation is evident for edge-on systems at lower SNR, as indicated by the elongated shape of the black contour and its alignment with $g(m)$ strips. Such degeneracy is absent in the case of an edge-on binary at higher SNR, in which case the GW mass function becomes redundant and the NS mass can be determined solely from the GW observations. Regarding the constraints on m_{ns} , the results obtained from the $g(m) - f(m)$ constraint slightly underestimate the actual constraints derived from the joint GW and EM observations.

The second column of Figure 6 represents cases with an intermediate inclination angle $\cos \iota = 0.5$. The upper middle panel of Figure 6 shows a system with $\text{SNR} \approx 5$. If $f(m)$ is measured with an error bar $\pm 1\%$, $m_{\text{ns}} < 1.6 M_{\odot}$ and $m_{\text{ns}} > 2.5 M_{\odot}$ can be ruled out by both $g(m) - f(m)$ and $2D - f(m)$ at the 90% confidence level. For the lower middle panel of Figure 6, the SNR is approximately four times the previous case, and the corresponding constraints are $1.88\text{--}2.10 M_{\odot}$ for $g(m) - f(m)$ and $1.88\text{--}2.12 M_{\odot}$ for $2D - f(m)$, respectively, when $\delta_{\text{fm}} = 1\%$. The mass-inclination degeneracy from GW observation persists for both cases, with the $g(m)$ contour aligning nicely with the $m_{\text{NS}} - \cos \iota$ contour for the $\text{SNR} \approx 5$

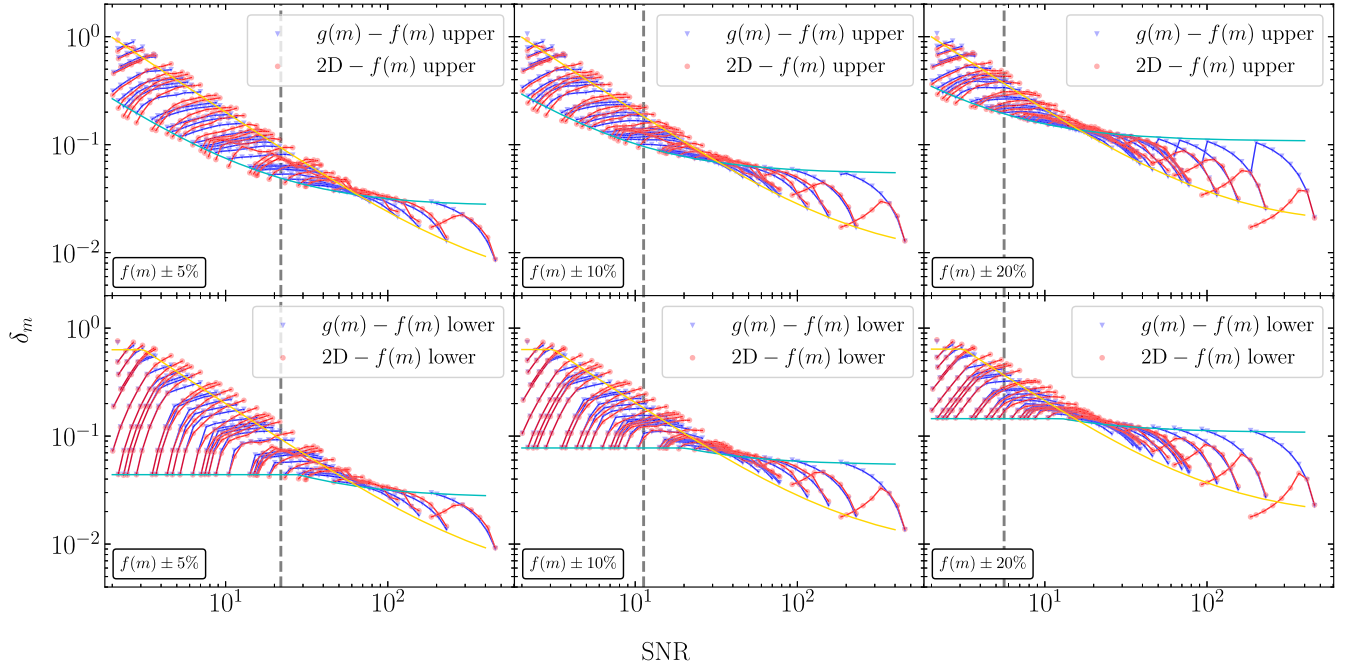


Figure 7. The relative size of the error bar of m_{NS} vs. the SNR of a wide range of NS–WD binaries with $P_{\text{orb}} = 20 - 60$ minutes, $\cos i = 0.1 - 0.9$, and $d = 1 - 12$ kpc. The upper panels show the upper bound $\delta_m^{\text{upper}} \equiv (m_{\text{NS,max}} - m_{\text{NS,0}})/m_{\text{NS,0}}$, and the lower panels show the lower bound $\delta_m^{\text{lower}} \equiv (m_{\text{NS,0}} - m_{\text{NS,min}})/m_{\text{NS,0}}$. The $g(m) - f(m)$ and $2D - f(m)$ constraints are calculated by finding the intersection of the 90% confidence intervals of the 1D PDF of $g(m)$ and the 2D PDF of $\cos i - m_{\text{NS}}$ with $f(m) \pm \delta_{\text{fm}}$, assuming $\delta_{\text{fm}} = 5\% - 20\%$. The vertical dashed lines represent the reference SNRs when $\delta_{\text{gm}} \approx \delta_{\text{fm}}$, and we have $\delta_{\text{gm}} \leq \delta_{\text{fm}}$ on the left-hand side of the dashed line. Systems of the same orbital period and distance but with different inclination angles are connected with solid lines, with nearly-edge-on systems (i.e., $\cos i = 0.1$) to the left and nearly-face-on systems $\cos i = 0.9$ to the right. The cyan (yellow) line in each panel represents the reference line calculated using Equation (A2) and Equation (11) for $\cos i = 0.1$ (0.9). As depicted in the figure, these reference lines distinctly trace the dependence of δ_m on SNR for systems with the respective inclination angles. The turning of the blue curve in the top right panel for high-SNR systems is due to the constraint imposed by $g(m)$ alone (Equation (14)).

case, and a slight mismatch for the $\text{SNR} \approx 10$ case at small m_{NS} , which are reminiscent of the first panel of this figure. In fact, the mass–inclination degeneracy gradually eases when $\text{SNR} \gtrsim 15$ and further disappears when $\text{SNR} \gtrsim 40$.

The third column represents nearly-face-on NS–WD binaries with $\cos i = 0.9$. For the $\text{SNR} \sim 5$ case, the 90% constraint on m_{NS} from $2D - f(m)$ is about $\pm 1 M_{\odot}$. In contrast, for the case with $\text{SNR} \sim 20$, the constraint narrows to around $\pm 0.24 M_{\odot}$ and remains insensitive to the value of δ_{fm} . Both constraints are much worse than those of intermediate inclination angles and near- $\pi/2$ inclination angles at the same SNR. For these nearly-face-on systems, the mass–inclination degeneracy persists even for systems with large SNR, which is evident from Figure 2. In fact, within the parameter space considered in this work, this degeneracy consistently persists for all systems with $\text{SNR} \leq 400$, implying its relevance for any realistic GW sources detectable by LISA. For the selected six systems, nearly-edge-on systems ($\cos i = 0.1$) have tighter constraints on m_{NS} compared to nearly-face-on systems ($\cos i = 0.9$) when the GW strength is comparable.

Similar parameter estimations were performed for a larger set of binaries with the same $m_{\text{NS}} = 2 M_{\odot}$, $m_c = 0.6 M_{\odot}$, with different orbital periods $P_{\text{orb}} = 20 - 60$ minutes located $d = 1 - 12$ kpc away, with inclination angles ranging from $\cos i = 0.1$ to $\cos i = 0.9$. The joint constraints on the NS mass are shown in Figure 7. For systems with SNR smaller than the reference SNR, $\delta_{\text{gm}} \geq \delta_{\text{fm}}$, the error bar δ_m is dominated by the uncertainty in the GW observation. Consequently, as explained in the previous section, the error bars for nearly-edge-on systems are slightly smaller compared

to those for nearly-face-on systems for the same orbital parameters, despite having a slightly larger SNR. The $g(m) - f(m)$ constraints (blue triangles) align with the joint constraints of $2D - f(m)$ (red circles), particularly for systems with small SNR. In this regime, the GW mass function captures the essence of the mass–inclination degeneracy, accurately reproducing and improving upon the joint constraints from multimessenger observations.

For systems with SNR much larger than the reference SNR, $\delta_{\text{gm}} \ll \delta_{\text{fm}}$, the GW amplitudes of the binary systems are sufficiently large, such that the constraints on NS mass are dominated by the uncertainty of the binary mass function $f(m)$. In this regime, the constraints on m_{NS} for edge-on systems outperform those for face-on systems. A significant discrepancy arises between the $g(m) - f(m)$ constraint and the $2D - f(m)$ constraint for systems with $\cos i \leq 0.5$ and $\text{SNR} \geq 100$, where the mass–inclination degeneracy has completely eased, as shown in the middle and right panels at large SNR in Figure 7.

The lower bounds of m_{NS} for systems with $\cos i \sim 0$ are much better than their upper bounds. This is due to the stringent constraint from $f(m)_{\text{min}}$ alone. When the error bars are much smaller than unity, the lower bounds are approximately $m_{\text{NS}} \geq 2 M_{\odot} \times \sin^3 i$.

As demonstrated by the systems discussed in this section, the mass constraints derived from the intersection of $g(m) - f(m)$ align closely with those obtained from the intersection of $2D - f(m)$ for NS–WD binaries with $\text{SNR} \lesssim 100$. Moreover, the former is accurately described by Equation (12) and the empirical relation of Equation (11). We can therefore conclude

that the proposed analytical formula for δ_{gm} , despite being an empirical relation, is well suited for estimating the mass constraints for NS–WD systems across a broad parameter range.

4. Discussions

4.1. GW Mass–Inclination Degeneracy

As pointed out in the previous section, the degeneracy between mass and inclination angle is prominent in systems with low SNR and it is reduced when SNR increases. For nearly-edge-on systems with $\cos i = 0.1$, the degeneracy would become less severe when $\text{SNR} \gtrsim 20$; for systems with an intermediate inclination of $\cos i = 0.5$, the degeneracy diminishes when $\text{SNR} \gtrsim 40$. However, for nearly-face-on systems with $\cos i = 0.9$, the degeneracy persists until $\text{SNR} \sim 400$.

The origin of this degeneracy lies in the indistinguishability of the two polarization modes, h_+ and h_\times , depending on both the SNR of the GW signal and the relative strength of the two modes. It is reminiscent of the distance–inclination degeneracy observed in the analysis of compact object binaries detected by the LIGO–Virgo–KAGRA (LVK) Scientific Collaboration network, which have been studied systematically by S. A. Usman et al. (2019). These two degeneracies both stem from the degeneracy between the GW amplitude and inclination angle (the $A-i$ degeneracy), albeit with subtle differences.

The $A-i$ degeneracy can be illustrated with the following example. Consider two L-shaped detectors oriented with a 45° offset, with $\psi = 0$ set to correspond to the configuration where the two detectors align with h_+ and h_\times , respectively. For an exactly face-on binary system with an arbitrary polarization angle, the signals recorded at both detectors are identical to those of a closer (or more massive) exactly edge-on system with $\psi = \pi/8$ (or $3\pi/8$, etc.), with the exception of a phase difference. An exactly edge-on system with a polarization angle slightly deviating from $\pi/8$ would therefore resemble a nearly-face-on system with an arbitrary polarization angle. In Bayesian inference, the range of each parameter is determined by marginalizing over the remaining parameters. Consequently, a nearly-edge-on system is prone to being misconstrued as a nearly-face-on system, whereas the reverse is not necessarily true. The relative strength of the two polarization modes $h_\times/h_+ \gtrsim 94\%$ for $\cos i \gtrsim 0.7$, suggesting that the GW signals from nearly-face-on systems become nearly indistinguishable from one another. This example elucidates the prominent degeneracy observed in Figure 2 and the $\cos i = 0.5$ and $\cos i = 0.9$ cases shown in Figure 6. Examining the system presented in Figure 2, where the injection parameter is $\cos i = 0.9$, the marginalized posterior of $\cos i$ extends toward both smaller and larger values, favoring $\cos i = 1$, as an exactly face-on template provides a decent fit to the signal, regardless of the polarization angle.

For a nearly-edge-on binary system, the degeneracy is reduced quickly as the SNR increases, and it disappears when $\text{SNR} \gtrsim 20$, a phenomenon also observed in LVK binaries. In LVK observations, when the network of GW detectors is equally sensitive to both polarization modes, the signals recorded in both detectors are dominated by the h_+ mode (except when ψ is very close to 0 or $\pi/4$). The relative strength of the two signals provides additional information about the polarization angle, which will aid in resolving the $A-i$

degeneracy. To be more precise, this measurement constrains $\phi - 2\psi$, as demonstrated in Figure 2.⁶

In the case of Galactic binaries, the situation is somewhat more intricate. Unlike the binaries observed by the LVK network, where the length of the GW signal is comparable to the binary orbital period (which allows for a precise estimation of ϕ), the observational time needed for the declaration of a detection is significantly longer than their orbital period for Galactic binaries. In the latter scenario, information about the initial orbital phase ϕ is lost, rendering it as a free orbital parameter. Due to the strong degeneracy between ψ and ϕ , ψ also becomes unconstrained. The upper panels of Figure 6 illustrate such cases. Regardless of the true inclination angle of the system, face-on templates almost always provide a decent fit to the signal, suggesting that the parameter estimation results tend to favor, or at least are consistent with, larger values of $\cos i$.

For systems with higher SNRs, the situation differs. As LISA rotates in space, the polarization angle varies with respect to the detector’s rest frame. Consequently, each TDI channel experiences at least one episode of high GW signal, when its orientation aligns exactly with h_+ , and one episode of low GW signal, when its orientation aligns with h_\times . This distinctive observational feature is absent in the low-SNR cases, due to the difficulty of signals being entangled with noise. Such a feature enables us to differentiate the amplitudes of two polarization modes, thereby constraining the system’s inclination angle. This condition corresponds to the cases in the bottom left panel of Figure 6.

4.2. Formation Channels of Compact NS–WD Binaries

Despite the prevalent belief (T. M. Tauris 2018; J.-G. He et al. 2024; V. Korol et al. 2024) that compact NS–WD systems that are observable with LISA could exist, there are no confirmed observations of such systems. Instead, the observed NS–WD binaries are typically found in much wider orbits.⁷ Therefore, it is worth discussing the possible formation channels for the specific binary systems of interest. NS–WD binaries are evolutionary end points of LMXBs/IMXBs, and a correlation between the post-LMXB orbital period and the WD mass is expected (see S. Rappaport et al. 1995; T. M. Tauris & G. J. Savonije 1999; A. G. Istrate et al. 2014), where systems with lighter WDs tend to have closer orbits. The post-LMXB/post-IMXB evolution is driven mainly by the loss of orbital angular momentum through gravitational radiation (see, e.g., B. Paczyński 1971), which constrains the initial orbital period of the binary as having to be $\lesssim 12$ hr in order for it to reach the LISA sensitivity band within a Hubble time. This narrow range of the initial orbital period and the correlation of the orbital period with the WD mass at the end of the LMXB/IMXB phase suggests that only those binaries with a WD mass smaller than $\lesssim 0.2 M_\odot$ can evolve toward this compactness relevant for GW observation (T. M. Tauris 2018), although the exact WD mass threshold depends on the mass and metallicity of the progenitor, the efficiency of the magnetic braking mechanism, and the initial orbital period in the pre-LMXB/pre-IMXB

⁶ The case presented here is nearly face-on, but this particular feature also exists for nearly-edge-on systems with low SNR. A similar degeneracy was discussed by S. A. Usman et al. (2019), although it was reported as $\phi \pm \psi$. Our additional factor of 2 is likely due to a difference in the convention of the polarization angle.

⁷ An up-to-date list of observed NS–WD binaries is available in the ATNF catalog: <https://www.atnf.csiro.au/research/pulsar/psrcat>.

phase (see, e.g., T. M. Tauris & G. J. Savonije 1999; W.-C. Chen et al. 2020; H.-L. Chen et al. 2021).

Alternatively, the NS may form after the WD, when the two progenitor stars in the initial binaries are massive enough (A. V. Tutukov & L. R. Yungel'Son 1993). This formation scenario was proposed to explain the origins of PSR B2303 +46 and PSR J1141–6545 (T. M. Tauris & T. Sennels 2000), and the resulting binary favors more massive WDs, i.e., CO or ONeMg WDs.

In dense nuclear stellar clusters or globular clusters where the stellar population is old, the terminating orbital period of the LMXB phase would be about a factor of 2 shorter than for those in the field (S. Rappaport et al. 1995). Moreover, the dense stellar environment underscores the significance of dynamical interactions. Compact NS–WD binaries might be produced through dynamical capture, three-body interactions, or even four-body interactions. Consider a binary with binding energy

$$E_b = \frac{Gm_{\text{ns}}^2 q}{2a} = \frac{G^{2/3}}{2} \left(\frac{2\pi}{P_{\text{orb}}} \right)^{2/3} m_{\text{ns}}^{5/3} \left[\frac{q}{(1+q)^{1/3}} \right], \quad (15)$$

where $q = m_2/m_{\text{ns}}$. The hardening rate of it is roughly

$$\frac{dE_b}{dt} \approx \xi G^2 \left(\frac{n_* \bar{m}^3}{\langle \sigma \rangle} \right) \quad (16)$$

(D. C. Heggie 1975), where $\xi \sim 10$, which includes contributions to binary hardening via wide/close three-body encounters, exchanges, and resonant encounters.⁸ \bar{m} represents the averaged mass of the encounters, n_* represents the stellar number density, and $\langle \sigma \rangle$ represents the velocity dispersion. The timescale it takes for an NS–WD binary to harden until the region where the GW dominates (i.e., when $P_{\text{orb}} \sim \text{days}$) is approximately (assuming $q = 0.4$)

$$T_{\text{harden}} = \frac{m_{\text{ns}}^{5/3}}{2\xi G^{4/3}} \frac{\langle \sigma \rangle}{n_* \bar{m}^3} \left(\frac{2\pi}{P_{\text{orb}}} \right)^{2/3} \frac{q}{(1+q)^{1/3}} \approx 26 \text{ Gyr} \left(\frac{m_{\text{ns}}}{2 M_\odot} \right)^{5/3} \left(\frac{10}{\xi} \right) \left(\frac{\langle \sigma \rangle}{200 \text{ km s}^{-1}} \right) \times \left(\frac{12 \text{ hr}}{P_{\text{orb}}} \right)^{2/3} \left(\frac{10^6 \text{ pc}^{-3}}{n_*} \right) \left(\frac{1 M_\odot}{\bar{m}} \right)^3, \quad (17)$$

which is about double the Hubble time. We have adopted a stellar density of $10^6 M_\odot \text{ pc}^{-3}$ at the inner 1 pc (D. Merritt 2010) of the Galactic center and a stellar velocity dispersion of 200 km s^{-1} . Similarly, for a typical globular cluster with a core stellar density of $\sim 10^4 M_\odot \text{ pc}^{-3}$ (J. A. Carballo-Bello et al. 2012; E. Pancino et al. 2017) and velocity dispersion of $\sim 5 \text{ km s}^{-1}$ (see, e.g., T. J. L. de Boer et al. 2019), the timescale for hardening is about five times the Hubble time.⁹ The hardening due to stellar encounters and subsequent

GW radiation would therefore be sufficient to produce the target NS–WD binaries if the binaries start off sufficiently hard themselves. Note that this hardening formula has included three-body exchange and resonant encounters, both of which tend to eject the least massive star among the triples. This process would likely produce an NS–WD binary with a heavier WD, the gravitational radiation for which is more efficient.

5. Conclusions

Compact NS–WD binaries potentially hold the most massive NSs. Measuring their masses is essential for our understanding of the densest matter in our Universe. In this work, we have studied the potential of using GW observations to measure the parameters of NS–WD binaries and proposed a novel multimessenger method to constrain the NS masses in these systems by combining the GW and EM detections. For a series of hypothetical NS–WD binaries with subhourly orbital period inside our Galaxy, we generated 4 yr of mock GW data for each system and performed parameter estimation using the `gbmcmc` package. By combining the GW information with the binary mass function from the EM observation, the degeneracy between the mass and inclination angle can be resolved, allowing for much tighter constraints on the NS mass. We showed that for our multimessenger method, the major factors that determine the constraint on the NS mass are the GW SNR of the NS–WD binary, the accuracy of the binary mass function, and the inclination angle. In general, for a realistic range of SNRs (i.e., ≤ 100), edge-on systems are favored over face-on systems in terms of parameter estimation.

Regardless of the inclination of the systems, our method suggests that the m_{ns} of an NS–WD binary can be constrained to within $\pm 0.2 M_\odot$, as long as their SNR ≥ 25 and the binary mass function is measured within $\pm 10\%$ accuracy. For an NS–WD binary with $P_{\text{orb}} \sim 60$ minutes and $m_c = 0.6 M_\odot$, the system needs to be within ~ 1 kpc. However, for a system with $P_{\text{orb}} \sim 20$ minutes, the distance threshold for the acceptable mass determination is about ~ 20 kpc. Our study suggests that those NS–WD binaries in globular clusters and in our Galaxy can be used to constrain the mass of massive NSs.

Last but not least, we defined a new concept: the GW mass function $g(m)$, which is derived from GW observations, in contrast to the binary mass function, which is derived from optical photometric or spectroscopy observations. We showed that the error bar of the GW mass function follows a simple power-law relation with the GW SNR of NS–WD binaries, regardless of the companion's mass, the orbital period, or the viewing inclination, validating the universality of this definition. Moreover, the GW mass function captures the essence of the mass–inclination angle degeneracy in GW observations and therefore serves as a handy tool for constraining m_{ns} with multimessenger observations.

Acknowledgments

We thank the anonymous referee of a previous paper of ours for encouraging us to fully develop the conceptual framework of the GW mass function. We thank Silvia Zane for the discussions on the mass–radius relations of NSs and various tests in future X-ray studies, Daisuke Kawata for those on stellar populations and the density at the Galactic center, and Qin Han for those on the evolution of compact binaries. We also thank Jane Yap, Joana Teixeira, and Jun Lau for general

⁸ We have dropped the dependency of the results on the mass ratio for simplicity, given that all the masses considered here are on the order of unity.

⁹ In the calculations, we set $\bar{m}/M_\odot = 1$, but stars in the nuclear star cluster of the Galactic center (see Z. Chen et al. 2023) and in globular clusters are old stars with masses well below $1 M_\odot$. Using a more accurate value for \bar{m}/M_\odot , however, would not alter the conclusion that hardening would take much longer than the Hubble time.

discussions and comments on this work. K.W. is grateful for the hospitality of NTHU IoA, where a substantial part of this work was conducted, during his visits. K.J.L. is supported by a PhD Scholarship from the Vinson and Cissy Chu Foundation and by a UCL MAPS Dean's Prize. K.W. and J.S.L. acknowledge the support of the UCL Cosmoparticle Initiative. This work is supported by the National Science and Technology Council of the Republic of China (Taiwan) under the grants 110-2628-M-007-005 and 113-2112-M-007-001 (PI: A. Kong). This work has made use of the NASA Astrophysics Data System.

Software: GetDist (A. Lewis 2019), Astropy (Astropy Collaboration et al. 2022), gbmcmc (T. B. Littenberg et al. 2020a), Mathematica (Wolfram Research, Inc. 2025).

Appendix Remarks on Assumptions and Error Propagation

The purpose of this study is to demonstrate the potential of utilizing GW observations to constrain the NS mass in conjunction with EM observations. Therefore, we have not incorporated uncertainties in the distance to the system and in the mass of the WD. For a more rigorous analysis, these uncertainties must be explicitly included in the error propagation.

For those WDs that are sufficient bright in the optical wave bands, Gaia can provide accurate distance measurements. To determine the mass of a WD, as an isolated source in the field or as a component star in a binary, is less straightforward. The most widely adopted method for WD mass determination relies on the measurement of surface gravity and effective temperature, by fitting spectroscopic data with atmospheric models (see, e.g., J. B. Holberg et al. 1985, 1986; P. Bergeron et al. 1992; A. Bragaglia et al. 1995; H. Schmidt 1996; D. S. Finley et al. 1997; M. A. Barstow et al. 2001; S. O. Kepler et al. 2017). The results, combined with a theoretical mass–radius relation for a finite-temperature WD structure (see, e.g., L. G. Althaus et al. 2005; I. Renedo et al. 2010; A. D. Romero et al. 2015), enable reasonably accurate mass inferences. A complication is whether the WD in NS–WD binaries would adhere to this evolutionary mass–radius relation, particularly in the presence of tidal effects and potential pulsar irradiation. However, when an accurate distance measurement is available, combining the WD luminosity with effective temperature information allows the deduction of the radius and, consequently, mass without detailed modeling of atmospheric physics (D. Koester et al. 1979; A. Bédard et al. 2017; C. Genest-Beaulieu & P. Bergeron 2019). Conversely, this method can also be used to derive the distance to the binary when combined with a surface gravity measurement if an accurate parallax measurement is unavailable. If the WD undergoes a certain evolutionary phase, pulsation mode analysis provides accurate mass measurements (see, e.g., S. D. Kawaler 1990; P. A. Bradley & D. E. Winget 1994; A. H. Córscico et al. 2019).

While a detailed analysis of the accuracy and systematics in mass and distance determinations is beyond the scope of this work, we still include here a recipe for error propagation appropriate for applications in real observations. When the error bars are much smaller than unity, we can write $d = d_0(1 \pm \delta_d)$, where d_0 represents the true value of the distance and δ_d represents the relative size of its error bar. The error of the distance enters the

GW mass function via

$$\delta_{\text{gm, re}} = \delta_{\text{gm}} + \frac{3}{5}\delta_d, \quad (\text{A1})$$

where $\delta_{\text{gm, re}}$ represents the realistic relative error bar of $g(m)$, and δ_{gm} represents the case with known distance (as used in the main text of this paper). Therefore, a 10% uncertainty of the distance translates into a 10% uncertainty of m_{ns} , approximately.





The companion mass does not enter the GW parameter estimation process, and therefore it does not affect the derived uncertainty of the GW mass function, even if it is unknown. However, its uncertainty will affect the constraint on the NS mass, as its value is used to derive m_{ns} from the intersection of two mass functions. We suppose that the companion's mass $m_c = m_{c,0}(1 \pm \delta_c)$.

When all system parameters are measured with errors much smaller than unity, Equation (12) can be approximately solved using series expansion. Keeping all errors to the leading order, the relative error on the NS mass can be approximated as

$$\begin{aligned} \delta_m &= C_{\text{gm}}\delta_{\text{gm, re}} + C_{\text{fm}}\delta_{\text{fm}} + C_c\delta_c, \\ &= \frac{1}{32(\cos 2\iota_0 + 3)m_{\text{ns},0} - 3m_{c,0}(-4\cos 2\iota_0 + \cos 4\iota_0 - 61)} \\ &\quad \times \{8\sin^2\iota_0(\cos 2\iota_0 + 7)(m_{c,0} + m_{\text{ns},0})\delta_{\text{fm}} \\ &\quad + 5(28\cos 2\iota_0 + \cos 4\iota_0 + 35)(m_{c,0} + m_{\text{ns},0})\left(\delta_{\text{gm}} + \frac{3}{5}\delta_d\right) \\ &\quad - [2m_{c,0}(52\cos 2\iota_0 + 3\cos 4\iota_0 + 9) + 3(28\cos 2\iota_0 \\ &\quad + \cos 4\iota_0 + 35)m_{\text{ns},0}]\delta_c\}, \end{aligned} \quad (\text{A2})$$

where $C_{\text{gm}}\delta_{\text{gm, re}}$ and $C_{\text{fm}}\delta_{\text{fm}}$ are the contribution from $f(m)$ and $g(m)$, and $C_c\delta_c$ is the contribution from m_c . The coefficient $C_c \in [-0.28, 0]$ for edge-on systems and ~ -1.3 for face-on systems when $m_{c,0} = [0.1, 0.6] M_\odot$. Note that the orders of magnitude of all coefficients (C) are unity, indicating that the uncertainty in m_{ns} will be dominated by the measurement with the greatest uncertainty δ . To utilize this method for the precise determination of the NS mass, accurate measurements of distance and the WD mass are necessary.

ORCID iDs

Kaye Jiale Li  <https://orcid.org/0000-0002-1657-0265>
 Jane SiNan Long  <https://orcid.org/0000-0002-2126-0050>
 Kinwah Wu  <https://orcid.org/0000-0002-7568-8765>
 Albert K. H. Kong  <https://orcid.org/0000-0002-5105-344X>

References

- Akmal, A., Pandharipande, V. R., & Ravenhall, D. G. 1998, *PhRvC*, **58**, 1804
- Alford, M. G., Han, S., & Prakash, M. 2013, *PhRvD*, **88**, 083013
- Althaus, L. G., García-Berro, E., Isern, J., & Córscico, A. H. 2005, *A&A*, **441**, 689
- Amaro-Seoane, P., Audley, H., Babak, S., et al. 2017, arXiv:1702.00786
- Antoniadis, J., Freire, P. C. C., Wex, N., et al. 2013, *Sci*, **340**, 448
- Astropy Collaboration, Price-Whelan, A. M., Lim, P. L., et al. 2022, *ApJ*, **935**, 167
- Avancini, S. S., Menezes, D. P., Alloy, M. D., et al. 2008, *PhRvC*, **78**, 015802
- Baldo, M., Burgio, G. F., & Schulze, H. J. 2000, *PhRvC*, **61**, 055801
- Barstow, M. A., Holberg, J. B., Hubeny, I., et al. 2001, *MNRAS*, **328**, 211
- Baym, G., Hatsuda, T., Kojo, T., et al. 2018, *RPPH*, **81**, 056902
- Bédard, A., Bergeron, P., & Fontaine, G. 2017, *ApJ*, **848**, 11
- Benacquista, M. J., Portegies Zwart, S., & Rasio, F. A. 2001, *CQGra*, **18**, 4025
- Bergeron, P., Saffer, R. A., & Liebert, J. 1992, *ApJ*, **394**, 228

- Bradley, P. A., & Winget, D. E. 1994, *ApJ*, **430**, 850
- Bragaglia, A., Renzini, A., & Bergeron, P. 1995, *ApJ*, **443**, 735
- Burdge, K. B., Coughlin, M. W., Fuller, J., et al. 2019, *Natur*, **571**, 528
- Burdge, K. B., Prince, T. A., Fuller, J., et al. 2020, *ApJ*, **905**, 32
- Carballo-Bello, J. A., Gieles, M., Sollima, A., et al. 2012, *MNRAS*, **419**, 14
- Char, P., & Banik, S. 2014, *PhRvC*, **90**, 015801
- Chen, H.-L., Tauris, T. M., Chen, X., & Han, Z. 2022, *ApJ*, **930**, 134
- Chen, H.-L., Tauris, T. M., Han, Z., & Chen, X. 2021, *MNRAS*, **503**, 3540
- Chen, W.-C., Liu, D.-D., & Wang, B. 2020, *ApJL*, **900**, L8
- Chen, Z., Do, T., Ghez, A. M., et al. 2023, *ApJ*, **944**, 79
- Cooray, A. 2004, *MNRAS*, **354**, 25
- Córsico, A. H., Althaus, L. G., Miller Bertolami, M. M., & Kepler, S. O. 2019, *A&ARv*, **27**, 7
- Cromartie, H. T., Fonseca, E., Ransom, S. M., et al. 2020, *NatAs*, **4**, 72
- de Boer, T. J. L., Gieles, M., Balbinot, E., et al. 2019, *MNRAS*, **485**, 4906
- Demorest, P. B., Pennucci, T., Ransom, S. M., Roberts, M. S. E., & Hessels, J. W. T. 2010, *Natur*, **467**, 1081
- Espino, P. L., & Paschalidis, V. 2019, *PhRvD*, **99**, 083017
- Finch, E., Bartolucci, G., Chuchenko, D., et al. 2023, *MNRAS*, **522**, 5358
- Finley, D. S., Koester, D., & Basri, G. 1997, *ApJ*, **488**, 375
- Finn, L. S., & Thorne, K. S. 2000, *PhRvD*, **62**, 124021
- Flanagan, É. É., & Hughes, S. A. 1998, *PhRvD*, **57**, 4535
- Fonseca, E., Cromartie, H. T., Pennucci, T. T., et al. 2021, *ApJL*, **915**, L12
- Genest-Beaulieu, C., & Bergeron, P. 2019, *ApJ*, **871**, 169
- Ghazanfari Mojarad, M., & Arabsaeidi, R. 2016, *IMPE*, **25**, 1650102
- He, J.-G., Shao, Y., Xu, X.-J., & Li, X.-D. 2024, *MNRAS*, **529**, 1886
- Heggie, D. C. 1975, *MNRAS*, **173**, 729
- Holberg, J. B., Wesemael, F., & Basile, J. 1986, *ApJ*, **306**, 629
- Holberg, J. B., Wesemael, F., Wegner, G., & Bruhweiler, F. C. 1985, *ApJ*, **293**, 294
- Istrate, A. G., Tauris, T. M., & Langer, N. 2014, *A&A*, **571**, A45
- Johnson, P. T., Coughlin, M. W., Hamilton, A., et al. 2023, *MNRAS*, **525**, 4121
- Kawaler, S. D. 1990, in ASP Conf. Ser. 11, Confrontation Between Stellar Pulsation and Evolution, ed. C. Cacciari & G. Clementini (San Francisco, CA: ASP), **494**
- Kepler, S. O., Koester, D., Romero, A. D., Ourique, G., & Pelisoli, I. 2017, in ASP Conf. Ser. 509, 20th European White Dwarf Workshop, ed. P. E. Tremblay, B. Gaensicke, & T. Marsh (San Francisco, CA: ASP), **421**
- Kilic, M., Brown, W. R., Bédard, A., & Kosakowski, A. 2021, *ApJL*, **918**, L14
- Koester, D., Schulz, H., & Weidemann, V. 1979, *A&A*, **76**, 262
- Korol, V., Igoshev, A. P., Toonen, S., et al. 2024, *MNRAS*, **530**, 844
- Korol, V., Rossi, E. M., Groot, P. J., et al. 2017, *MNRAS*, **470**, 1894
- Kupfer, T., Korol, V., Shah, S., et al. 2018, *MNRAS*, **480**, 302
- Kupfer, T., Korol, V., Littenberg, T. B., et al. 2024, *ApJ*, **963**, 100
- Lattimer, J. M., & Prakash, M. 2004, *Sci*, **304**, 536
- Lattimer, J. M., & Prakash, M. 2007, *PhR*, **442**, 109
- Lattimer, J. M., & Prakash, M. 2011, in From Nuclei to Stars: Festschrift in Honor of Gerald E Brown, ed. Sabine Lee (Singapore: World Scientific), **275**
- Lattimer, J. M., & Swesty, D. F. 1991, *NuPhA*, **535**, 331
- Lewis, A., 2019 GetDist: A Python Package for Analysing Monte Carlo Samples, <https://github.com/cmbant/getdist>
- Li, A., Miao, Z., Han, S., & Zhang, B. 2021, *ApJ*, **913**, 27
- Li, Z. H., & Schulze, H. J. 2008, *PhRvC*, **78**, 028801
- Littenberg, T. B., & Cornish, N. J. 2019, *ApJL*, **881**, L43
- Littenberg, T. B., Cornish, N. J., Lackeos, K., & Robson, T., 2020a tlittenberg/ldasoft: Preliminary Release, v0.0-beta, Zenodo, doi:[10.5281/zenodo.2026177](https://doi.org/10.5281/zenodo.2026177)
- Littenberg, T. B., Cornish, N. J., Lackeos, K., & Robson, T. 2020b, *PhRvD*, **101**, 123021
- Maggiore, M. 2008, Gravitational Waves: Theory and Experiments, Vol. 1 (Oxford: Oxford Univ. Press)
- Merritt, D. 2010, *ApJ*, **718**, 739
- Mickaelian, A. M., Mikayelyan, G. A., Abrahamyan, H. V., Paronyan, G. M., & Malkov, O. Y. 2022, *OAst*, **30**, 210
- Moore, C. J., Cole, R. H., & Berry, C. P. L. 2015, *CQGra*, **32**, 015014
- Moshfegh, H. R., & Ghazanfari Mojarad, M. 2013, *EPJA*, **49**, 1
- Nelemans, G., Yungelson, L. R., & Portegies Zwart, S. F. 2001, *A&A*, **375**, 890
- Paczynski, B. 1971, *ARA&A*, **9**, 183
- Pancino, E., Bellazzini, M., Giuffrida, G., & Marinoni, S. 2017, *MNRAS*, **467**, 412
- Pang, P. T. H., Tews, I., Coughlin, M. W., et al. 2021, *ApJ*, **922**, 14
- Rappaport, S., Podsiadlowski, P., Joss, P. C., Di Stefano, R., & Han, Z. 1995, *MNRAS*, **273**, 731
- Reddy, V., Kelley, M. S., Farnocchia, D., et al. 2019, *Icar*, **326**, 133
- Renedo, I., Althaus, L. G., Miller Bertolami, M. M., et al. 2010, *ApJ*, **717**, 183
- Robson, T., Cornish, N. J., & Liu, C. 2019, *CQGra*, **36**, 105011
- Romero, A. D., Campos, F., & Kepler, S. O. 2015, *MNRAS*, **450**, 3708
- Schmidt, H. 1996, *A&A*, **311**, 852
- Stroeer, A., & Vecchio, A. 2006, *CQGra*, **23**, S809
- Tan, H., Dore, T., Dexheimer, V., Noronha-Hostler, J., & Yunes, N. 2022, *PhRvD*, **105**, 023018
- Tang, S.-P., Jiang, J.-L., Han, M.-Z., Fan, Y.-Z., & Wei, D.-M. 2021, *PhRvD*, **104**, 063032
- Tauris, T. M. 2018, *PhRvL*, **121**, 131105
- Tauris, T. M., & Savonije, G. J. 1999, *A&A*, **350**, 928
- Tauris, T. M., & Sennels, T. 2000, *A&A*, **355**, 236
- Tutukov, A. V., & Yungel'son, L. R. 1993, *ARep*, **37**, 411
- Usman, S. A., Mills, J. C., & Fairhurst, S. 2019, *ApJ*, **877**, 82
- Vidaña, I., Logoteta, D., Providência, C., Polls, A., & Bombaci, I. 2011, *EL*, **94**, 11002
- Wolfram Research, Inc., 2025 Mathematica, v14.2, <https://www.wolfram.com/Mathematica>
- Yu, S., Lu, Y., & Jeffery, C. S. 2021, *MNRAS*, **503**, 2776
- Zhou, X. R., Burgio, G. F., Lombardo, U., Schulze, H. J., & Zuo, W. 2004, *PhRvC*, **69**, 018801
- Zurair, Z., Mukhopadhyay, B., & Weber, F. 2023, *ARep*, **67**, S199